

DTIC  
ELECTE  
AUG 07 1990  
D<sub>CS</sub> D

①

AD-A225 135

DTIC FILE COPY

## Experimental and Theoretical Study of Rayleigh-Lamb Waves in a Plate Containing a Surface-Breaking Crack

Joseph Paffenholz,<sup>1</sup> Jon W. Fox,<sup>2</sup> Xiaobai Gu,<sup>3</sup> Greg S. Jewett,<sup>4</sup>  
Subhendu K. Datta,<sup>5</sup> Hartmut A. Spetzler<sup>6</sup>

<sup>1,4,5,6</sup> Cooperative Institute for Research in Environmental Sciences, University of Colorado, Boulder, CO 80309-0216, USA; <sup>2,3,5</sup> Department of mechanical Engineering, University of Colorado, Boulder, CO 80309-0427, USA; and <sup>6</sup> Department of Geological Sciences, University of Colorado, Boulder, CO 80309-0250, USA

**Abstract.** Scattering of Rayleigh-Lamb waves by a normal surface-breaking crack in a plate has been studied both theoretically and experimentally. The two-dimensionality of the far field, generated by a ball impact source, is exploited to characterize the source function using a direct integration technique. The scattering of waves generated by this impact source by the crack is subsequently solved by employing a Green's function integral expression for the scattered field coupled with a finite element representation of the near field. It is shown that theoretical results of plate response, both in frequency and time, are similar to those obtained experimentally. Additionally, implications for practical applications are discussed. *Reprints: 160*

### DISTRIBUTION STATEMENT A

Approved for public release  
Distribution unlimited

### Introduction

Propagation of guided Rayleigh-Lamb waves in a plate is of interest in seismology, electrical devices, ultrasonic material characterization, and ultrasonic nondestructive evaluation of defects. There have been numerous investigations of this problem since the early works of Rayleigh and Lamb, and reviews of the early literature can be found [1, 2]. In recent years attention has been focused on the surface response of a plate due to buried or surface sources in the context of acoustic emission. The direct problem of the response of a plate due to various sources has been studied by many authors [3-10] for the purpose of analyzing signals from acoustic emissions. Experimental measurements of surface response due to normal force sources acting on a plate have also been examined [10-16]. In this paper we have theoretically studied the surface response of a plate due to a vertical transient line force acting on the surface of the plate. The problem is considered to be two-dimensional, i.e., plane strain. The model studied is a simulation of the experimental set-up shown in Fig. 1.

032

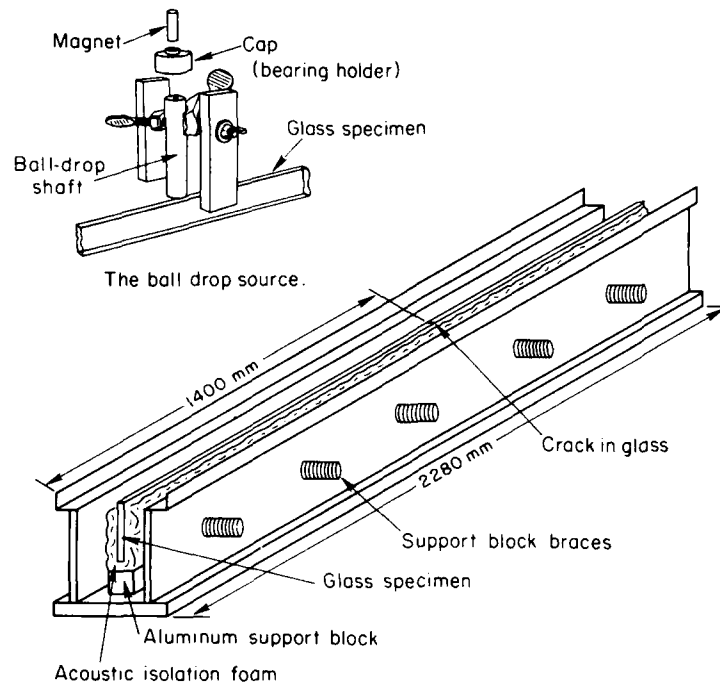


**Fig. 1.** The glass specimen with support structure and ball drop source apparatus. The structure supports the 25.4 mm by 5.6 mm by 2.28 m specimen but is mechanically decoupled by a high attenuation, impedance mismatch urethane foam. This minimizes the loss of energy to the supporting structure while isolating the specimen from external vibrations. Aluminum coated microscope slides are glued to the sample surface to provide the electrically conductive and smooth surface required by the sensor.

### Theoretical Formulation and Solution

The response of an elastic plate due to an applied source of excitation is characterized by the type of source. Theoretical knowledge of response due to known sources helps in identifying source functions generated in experimental set-ups, or in practical applications. Characterizing a physical source in a numerical form is a necessary step towards analyzing the scattered field for nondestructive evaluation of defects in a plate.

The propagation of waves in elastic plates has long been studied by many authors. Mindlin [1] gave a thorough discussion of the solutions to the governing equations of wave propagation in isotropic plates. Since then, many studies have been reported on the forced motion of a plate. Recently transient wave propagation in an infinite plate due to a point source was studied by Ceranoglu and Pao [2]. They employed a generalized ray theory to compute the desired response; however, this method is very cumbersome when considering responses in the far field, i.e., several plate thicknesses away from the source. To avoid this difficulty Weaver and Pao [8] used a normal mode analysis to analyze responses in the far field. The response of a finite plate was described by a

double summation over wave number and eigenfrequencies. Letting the radius approach infinity, the summation over wave number gets replaced by its indefinite integral. Vasudevan and Mal [9] presented a method based on the classical integral transform technique. The response at a particular frequency is obtained by using the method of residues at the poles (real, imaginary, and complex) which represent the modes of propagation discussed in [1]. Finally, an inverse fast-Fourier-transform (FFT) is used to obtain the time response of the plate.

In this work we consider the two-dimensional problem of a uniform line force acting on one face of a plate. The response of the plate due to an impulsive load is written in the form of a double integral over the frequency and wave number. For any frequency, direct integration is carried out with respect to the real wave number after adding a small imaginary part to the real frequency. The Fourier spectrum of the experimentally generated source function is then obtained by calculating the ratio of the observed response and the input response. The corresponding representation in time domain is then carried out by taking the inverse FFT of the frequency response. This numerical representation of the source function is used to study the scattering of waves by a normal surface crack in a plate.

### Evaluation of Green's Function

The Green's function for a medium,  $G_{ij}(x, z, t; x', z', 0)$ , is defined as the displacement in the  $i^{\text{th}}$  direction produced at a point  $(x, z)$  at time  $t$  by an impulsive line force of unit magnitude acting at  $t = 0$  in the  $j^{\text{th}}$  direction. For computing  $G_{ij}$  we consider the source to be uniform along the  $y$ -axis, i.e., we assume the problem to be a 2-D plane strain problem. In index notation the Green's displacement vector  $\mathbf{G}_j$  must satisfy the equation of motion:

$$\mu \nabla^2 \mathbf{G}_j + (\lambda + \mu) \nabla \nabla \cdot \mathbf{G}_j = \rho \ddot{\mathbf{G}}_j - \mathbf{e}_j \delta(t) \delta(x - x') \delta(z - z'), j = 1, 3. \quad (1)$$

Assuming the displacement vector to be of the form

$$\mathbf{G}_j = \nabla \phi_j + \nabla \Lambda(\psi_j \mathbf{e}_2), \quad (2)$$

one gets

$$\begin{aligned} G_{1j} &= \frac{\partial \phi_j}{\partial x} - \frac{\partial \psi_j}{\partial z} \\ G_{3j} &= \frac{\partial \phi_j}{\partial z} + \frac{\partial \psi_j}{\partial x}, \end{aligned} \quad (3)$$

where  $\phi_j$  and  $\psi_j$  satisfy the differential equations (except at  $x', z'$ ):

$$\begin{aligned} \nabla^2 \phi_j &= \frac{1}{C_1^2} \ddot{\phi}_j, \quad \nabla^2 \psi_j = \frac{1}{C_2^2} \ddot{\psi}_j, \\ C_1^2 &= (\lambda + 2\mu)/\rho, \quad C_2^2 = \mu/\rho. \end{aligned}$$

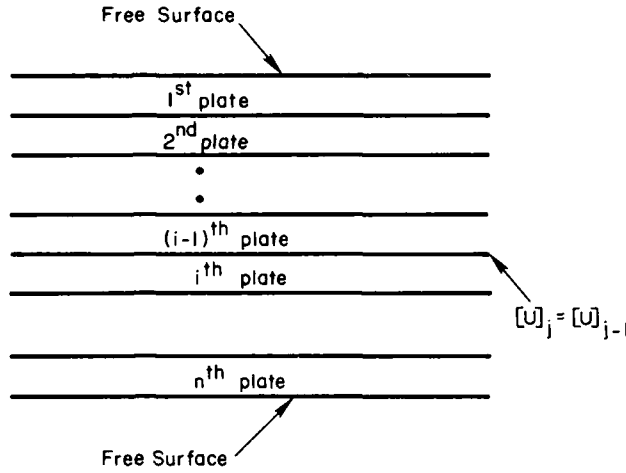


**Fig. 2.** Two-dimensional layered plate with top and bottom surfaces traction free. The layered plate contains  $n$  plates of thickness  $h$ , welded together with total thickness of  $nh = H$ .

For generality, let us consider  $n$  plates of equal thickness  $h$  that are welded together with the top and bottom surfaces being traction free (See Fig. 2). In order to solve for the Green's displacement,  $\mathbf{G}_j$ , in the  $n$ -layered plate we take the time dependence first in the form  $e^{-i\omega t}$ , where  $\omega$  is circular frequency. Furthermore, we write

$$\Phi_j = \int_{-\infty}^{\infty} \phi_j e^{ikx} dx$$

$$\Psi_j = \int_{-\infty}^{\infty} \psi_j e^{ikx} dx. \quad (4)$$

Then it is easily shown that within the  $m^{\text{th}}$  layer  $\Phi_j$  and  $\Psi_j$  can be written as

$$\Phi_j^m = A_j^m e^{i\eta_{1m}z} + B_j^m e^{i\eta_{2m}(h-z)} + S_j^m \quad (5)$$

$$\Psi_j^m = A_j^m e^{i\eta_{1m}z} + B_j^m e^{i\eta_{2m}(h-z)} + S_j^m, \quad (6)$$

where

$$\eta_{1m} = \sqrt{k_{1m}^2 - k^2}, \quad \eta_{2m} = \sqrt{k_{2m}^2 - k^2},$$

$$k_{1m} = \omega/C_{1m}, \quad k_{2m} = \omega/C_{2m}$$

$S_j^m$  and  $T_j^m$  depend on the direction and location of the applied unit load. For a force in the  $z$ -direction acting at  $(x', z')$  they are described as

$$S_3^m = \pm A^{3m} e^{i\eta_{1m}|z-z'|}$$

$$T_3^m = B^{3m} e^{i\eta_{2m}|z-z'|} \quad (7)$$

where

$$A^{3m} = \frac{e^{-ikx'}}{(2\mu_m k_{2m}^2)}, B^{3m} = \frac{K}{\eta_{2m}} \frac{e^{-ikx'}}{(2\mu_m k_{2m}^2)}.$$

In the above the  $\pm$  signs correspond to  $z >$  or  $< z'$ , respectively. Similarly, for a force in the  $x$ -direction at  $(x', z')$  we get

$$\begin{aligned} S_1^m &= A^{1m} e^{i\eta_{1m}|z-z'|} \\ T_1^m &= \pm B^{1m} e^{i\eta_{2m}|z-z'|} \end{aligned} \quad (8)$$

with

$$A^{1m} = \frac{K}{\eta_{1m}} \frac{e^{-ikx'}}{(2\mu_m k_{2m}^2)}, B^{1m} = \frac{-e^{-ikx'}}{(2\mu_m k_{2m}^2)}.$$

If there is no applied load in the  $m^{\text{th}}$  layer, then  $S_j^m = T_j^m = 0$ . Note that in writing the above solution a local coordinate system has been chosen with the origin on the top of the layer.

The stresses associated with the Green's displacement  $\mathbf{G}_j^m$  are calculated from the stress-strain relations. The relevant stress components needed to satisfy the continuity conditions at the interface and the free-surface conditions are

$$\begin{aligned} \Sigma_{xzj}^m &= \mu_m \left( \frac{\partial}{\partial z} G_{zj}^m + \frac{\partial}{\partial x} G_{xj}^m \right) \\ \Sigma_{zzj}^m &= \lambda_m \nabla \cdot \mathbf{G}_j + 2\mu_m \frac{\partial}{\partial z} G_{zj}^m. \end{aligned} \quad (9)$$

Using Eqs. (5) and (6) in Eq. (3), and in Eq. (9), the Fourier transforms of the displacement-stress vector in the  $m^{\text{th}}$  layer can be written in matrix form as

$$[U_j^m(z)] = [l^m(z)][X_j^m] + [Y_j^m], \quad (10)$$

where

$$\begin{aligned} [U_j^m(z)] &= [\hat{G}_{xj}^m, \hat{G}_{zj}^m, \hat{\Sigma}_{zzj}^m, \hat{\Sigma}_{xzj}^m]^T \\ [X_j] &= [A_j^m C_j^m B_j^m D_j^m]^T \end{aligned}$$

Expressions for  $l^m$  and  $Y_j^m$  are given in Appendix I. The  $\hat{f}$  represents the Fourier transform of  $f(x)$ .

The boundary conditions to be satisfied by  $[U_j]$  are

$$\hat{\Sigma}_{zzj}^l = \hat{\Sigma}_{xzj}^l = 0 \text{ at } z = 0 \quad (11)$$

$$[U_f^m(h)] = [U_f^{m+1}(0)], \quad m = 1, \dots, n-1 \quad (12)$$

$$\hat{\Sigma}_{zz}^n = \hat{\Sigma}_{xz}^n = 0 \text{ at } z = h \quad (13)$$

These give  $4n$  conditions for the  $4n$  unknown constants  $[X_f^m]$ ,  $m = 1, \dots, n$ .

Assembling the Eqs. (11)–(13) into a global matrix we obtain the matrix equation

$$[F][X] = [Y] \quad (14)$$

where  $[F]$  is a  $4n \times 4n$  matrix,

$$[X] = [A_j^1, C_j^1, B_j^1, D_j^1, \dots, A_j^n, C_j^n, B_j^n, D_j^n]^T \text{ and } [Y] = [YY_1, \dots, YY_{n+1}]^T$$

with

$$YY_1 = [-Y_j^1(3), -Y_j^1(4)]_{z=0}^T$$

$$YY_{n+1} = [-Y_j^n(3), -Y_j^n(4)]_{z=h}^T$$

$$YY_m = [Y_j^m|_{z=0} - Y_j^{m-1}|_{z=h}]^T, \quad m = 2, \dots, n.$$

Note that  $YY_1$  and  $YY_{n+1}$  are  $2 \times 1$  matrices and the rest are  $4 \times 1$ .

Solving Eq. (14) for  $[X]$  we obtain all of the constants. Once these constants are known the displacements and stresses at any point can be found. It may be noted that setting the determinant of  $[F]$  to zero gives the dispersion equation that relates the frequency  $k_{21}$  to the wave number  $k$ . This has been discussed recently by Mal [17].

### Extraction of the Source Function

We shall now focus our attention on a single homogeneous plate and obtain an expression for the  $z$ -component of the displacement at  $z = 0$  for a vertical load also acting at  $z = 0$ . This will be denoted by  $D(x, x', f)$  for a particular frequency  $\omega = 2\pi f$ ,  $f$  being measured in cycles per second. Following the procedure for an  $n$ -layered plate we get the four constants  $A_3^1$ ,  $C_3^1$ , and  $D_3^1$ . Using these constants we find from Eqs. (5), (6) and (3) (see also Achenbach [18]):

$$D(x, x'; f) = \frac{1}{2\pi} \int_{-\infty}^{\infty} \{l_{21}^1 A_3^1 + l_{22}^1 C_3^1 + l_{23}^1 B_3^1 + l_{24}^1 D_3^1 + Y_{23}^1\}_{z=z'=0} e^{ikx} dk \quad (15)$$

where  $A_3^1, \dots, D_3^1$  are the solutions to the equation

$$\begin{bmatrix} a & c & ae^{i\eta_{11}h} & -ce^{i\eta_{21}h} \\ b & -a & -be^{i\eta_{11}h} & -ae^{i\eta_{21}h} \\ ae^{i\eta_{11}h} & ce^{i\eta_{21}h} & a & -c \\ be^{i\eta_{11}h} & -ae^{i\eta_{21}h} & -b & -a \end{bmatrix} \begin{Bmatrix} A_3^1 \\ C_3^1 \\ B_3^1 \\ D_3^1 \end{Bmatrix} = \begin{Bmatrix} aA^{31} + cB^{31} \\ -bA^{31} + aB^{31} \\ aA^{31}e^{i\eta_{11}h} + cB^{31}e^{i\eta_{21}h} \\ -bA^{31}e^{i\eta_{11}h} + aB^{31}e^{i\eta_{21}h} \end{Bmatrix}$$

The integration is done numerically according to an adaptive scheme that is a modification of one by Xu and Mal [19]. Using this scheme we evaluate displacements and stresses as a function of  $k_2$  at any point  $(x, y)$  for a source at  $(x', z')$  in the plate. The results of integration were checked for some arbitrary frequencies with those obtained by the method of modal summation. In this particular problem, since the source and receiver are at the top surface,  $z$  and  $z'$  are zero.

Experimentally we measure the time responses of normal surface displacements at the receivers  $r_1$  and  $r_2$  that are distances  $d_1$  and  $d_2$  from the source, respectively. The source is considered to be a line source  $S$  uniform along the width of the plate and acting in the  $z$ -direction. We then obtain the corresponding frequency responses  $R_1(f)$  and  $R_2(f)$  by means of an FFT. Now, the response at a frequency  $f$ ,  $R(f)$  at the point  $(x, 0)$  is given by  $S(f)*D(f)$ , where  $S(f)$  is the frequency response of the source and  $D(f)$  is given by Eq. (15). We obtain  $D(f)$  analytically and hence, compute  $S(f)$  from the observed  $R(f)$ . Thus we get  $S$  for discrete frequencies  $f = n \times \Delta f$ , where  $n = 1, 2, \dots, m$ ,  $m = 2^l$ ,  $l$  an integer, and  $\Delta f = 1/T_f$ ,  $T_f$  being the length of the time window. This  $S(f)$ , which is a complex number, represents the source function in the frequency domain. The corresponding time representation of the source is obtained by taking the inverse FFT. For two different observation points the time signals measured by the receivers at  $(x_1, 0)$  and  $(x_2, 0)$  are labeled as  $T_1$  and  $T_2$ , respectively, with their corresponding frequency spectra as  $R_1(f)$  and  $R_2(f)$ . From the theoretically computed  $D_1(f)$  and  $D_2(f)$  at these points, since

$$S_1(f) = R_1(f)/D_1(f), \quad S_2(f) = R_2(f)/D_2(f),$$

we thereby obtain the source function from observations at different receiver positions. Since the source remains the same for both the receiver positions,  $S_1(f)$  and  $S_2(f)$  should be identical, at least in theory. In practice, they are found to agree extremely well when the receivers are more than a few plate thicknesses away, (i.e., more than  $3H$ ). Note that we did not evaluate the source functions at zero frequency, so the corresponding time representation of the source will have an inherent DC component.

The positions of the receivers considered in this work are  $x_1 = 5H$  and  $x_2 = 8H$ . Since the time signals do not decay sufficiently at the end of the time window, a window is used on the experimental time signals to force them to decay. The window used is  $\cos(i \pi/(2n))$ , where  $i = 1, 2, \dots, n$ ,  $n$  was taken to be 512. This window is imposed on all of the experimental time signals for computational purposes. Additionally, zero's were added to the time signals to increase the length of the signals by a factor of 2. This introduction of zero's enables the  $\Delta f$  to be reduced by a factor of 2, for increased numerical accuracy, without sacrificing the integrity of the information contained in the signal.

### Scattering by a Surface-Breaking Crack

The problem of scattering of incident body waves by a surface-breaking crack is solved by employing a hybrid method which combines the advantages of the

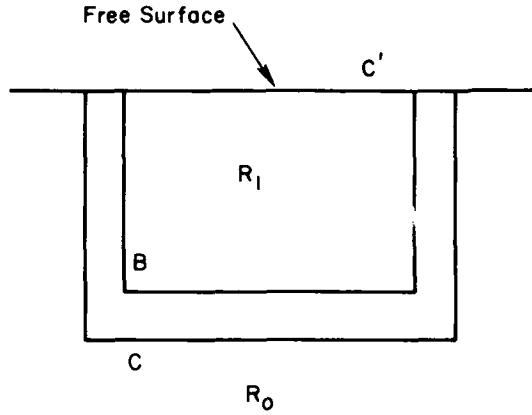


**Fig. 3.** Regions and boundaries used by the hybrid method which combines the advantages of the finite element technique and the boundary integral method. The boundaries are B and C, with C' being the free surface. The regions are  $R_1$  (interior) and  $R_0$  (exterior). The finite element mesh that is contained in  $R_1$  is illustrated in Fig. 7.

finite element technique and the boundary integral method. The details of the hybrid method are discussed by Khair et al. [20, 21], who considered scattering in a semi-infinite medium. For this purpose we consider two artificial boundaries  $C$  and  $B$  (Fig. 3). The medium is now divided into two regions. The interior region  $R_1$  is bounded by  $B$ , and the free surface. The exterior region  $R_0$  is bounded by the free surface, the boundary  $C$ , the boundary  $z = H$  and extends to infinity in the  $\pm x$  directions. The area between  $C$  and  $B$  is shared by both regions. In regions  $R_0$  and  $R_1$  the governing equation of elastic motion is written as, assuming the time dependence  $e^{-i\omega t}$ ,

$$T_{ij,j} + \rho \omega^2 U_i = 0, \quad i, j = 1, 3 \quad (16)$$

where  $T_{ij}$  is the stress tensor,  $\rho$  the mass density and  $U_i$  the  $i$ th displacement component. Solution to Eq. (16) satisfying the stress-free boundary conditions along the surface of the half-space and the crack surface is sought.

#### *Solution in the Exterior Region $R_0$*

In this region the displacement is composed of two parts.

$$U_i = U_i^{(0)} + U_i^{(s)} \quad (17)$$

where  $U_i^{(0)}$  ( $i = 1, 3$ ) represents the free field displacement components (the incident field due to the line load) and  $U_i^{(s)}$  is the scattered field. The scattered displacement field in  $R_0$  is represented by a surface integral [20], after dropping the factor  $e^{-i\omega t}$ ,

$$U_j^{(s)}(x', z') = \int_C (G_{ij} T_{ik} - U_i \Sigma_{ijk}) n_k dS \quad (18)$$

Here  $G_{ij}$  is the previously described Green's displacement tensor and  $n_k$  defines the components of the outward unit normal vector to  $C$ . The integration along  $C$  is carried out in the clockwise direction.



*Solution in the Interior Region  $R_I$* 

This region is divided into finite elements having  $N_I$  number of interior nodes and  $N_B$  number of boundary nodes. For the finite element representation in region  $R_I$  the energy functional is taken to be

$$E = 1/2 \iint_{R_I} [\mathbf{T} \cdot \boldsymbol{\epsilon}^* - \rho w^2 \mathbf{U} \cdot \mathbf{U}^*] dA - 1/2 \int_B [\mathbf{t}_B \cdot \mathbf{U}_B^* + \mathbf{t}_B^* \cdot \mathbf{U}_B] dS \quad (19)$$

where \* denotes complex conjugate and  $\mathbf{T}$ ,  $\boldsymbol{\epsilon}$  are stress and strain vectors defined as

$$\mathbf{T} = [T_{xx}, T_{zz}, T_{xz}]^T \quad (20)$$

$$\boldsymbol{\epsilon} = [\epsilon_{xx}, \epsilon_{zz}, \epsilon_{xz}]^T. \quad (21)$$

Superscript  $T$  denotes transpose.  $\mathbf{t}_B$  and  $\mathbf{U}_B$  denote the traction and displacement at contour  $B$ , respectively. It is assumed that the displacement field within an element is represented in terms of the shape functions  $\phi_i(x, z)$  and elemental nodal displacements  $U_{il}^{(e)}$  as

$$U_i^{(e)} = \sum_{l=1}^n \phi_l U_{il}^{(e)} \quad (i = 1, 3) \quad (22)$$

The number of nodes in each element is given by  $n$ . Substituting Eq. (22) into the strain-displacement relations and these, in turn into the stress-strain relations provides  $T_{ij}^{(e)}$  and  $\epsilon_{ij}^{(e)}$ . Substituting these in Eq. (19) and taking its variation, the equation of motion for region  $R_I$  can be written as

$$\begin{bmatrix} S_{II} & S_{IB} \\ S_{BI} & S_{BB} \end{bmatrix} \begin{Bmatrix} \mathbf{U}_I \\ \mathbf{U}_B \end{Bmatrix} = \begin{Bmatrix} 0 \\ \mathbf{Y}_B \end{Bmatrix} \quad (23)$$

The elemental impedance matrix  $[S]_e$  is given by

$$[S]_e = \int_{A_e} \{ [B_e^*]^T [D] [B_e] - \rho w^2 [\phi_e]^T [\phi_e] \} dA \quad (24)$$

and  $\mathbf{Y}_B$  is the nodal force vector due to surface tractions on the boundary. Using the top set of equations in Eq. (23) we get

$$[\mathbf{U}_I] = -[S_{II}]^{-1} [S_{IB}] \{\mathbf{U}_B\} \quad (25)$$

Matrices  $[B_e]$  and  $[D]$  have been derived before [20]. Combining Eqs. (18) and (25) the boundary displacement  $\mathbf{U}_B$  is found to be

$$\{\mathbf{U}_B\} = (-[A_{BI}][S_{II}]^{-1}[S_{IB}] + A_{BB})\{\mathbf{U}_B\} + \{\mathbf{U}_B^{(0)}\}. \quad (26)$$

Once  $\{\mathbf{U}_B\}$  is found by solving Eq. (26),  $\{\mathbf{U}_I\}$  is found from Eq. (25). The aforementioned method was used to solve for the  $Z$ -component of the surface

displacements in the presence of a normal surface-breaking crack when the plate is excited by a source on the same surface as the crack. The parameters used for Poisson's ratio, Young's modulus, and the  $P$  and  $SV$  velocities were those of standard window pane glass (see the following Experimental Procedure).

### **Experimental Procedure**

In the experimental part of this study we generate Rayleigh-Lamb waves in glass samples. Our purpose is two-fold. On the one hand we wish to create an approximation to the two-dimensional case which is theoretically tractable. Here we need to determine the source function and study the effect of a crack on the propagation of the waves in the far field. On the other hand we are exploring other possible experimental arrangements with the aim of producing a practical tool for crack detection. In these latter arrangements we do not limit ourselves to those configurations which lend themselves to theoretical treatments.

We will now describe the experimental apparatus which consists of the following parts: the source, the receiver, the sample, and the data acquisition system.

#### *The Source*

The source consists of 1.6 mm steel ball bearings impinging on the glass surface. The balls are dropped through a carefully reamed hole in a brass tube. The hole diameter is just slightly larger than the ball diameter to assure laminar air flow around the balls and thus reproducible ball impact velocities. The balls are held by a magnet and released by removing the magnetic field (Fig. 1).

#### *The Receiver*

Since we are comparing normal surface displacements obtained from experiments with theoretically derived results, a transducer (receiver) with a known transfer function is required, i.e., one with an absolute calibration of amplitude response versus frequency. We have developed such a transducer (see [22]), that alleviates many of the problems which exist with conventional piezoelectric transducers. Electronically this capacitive transducer (CT) is based on the VideoDisk player development by RCA (Radio Corporation of America). It detects the changes in a 100 nm gap between a 0.3 mm diameter needle and the surface of the sample. It responds only to the component of the signal that is normal to the surface. The frequency response is flat within 7 dB from below 10 kHz to above 6 MHz. The sensitivity of the instrument approaches that of piezoelectric transducers at 0.44 V/nm with a noise level of 0.004 volts. At a one to one signal to noise level, its absolute sensitivity is therefore about 0.015 nm. The dynamic range covers over three orders of magnitude from 0.015 nm to over 50 nm. The sensitivity of the CT is given in Fig. 4 as a function of

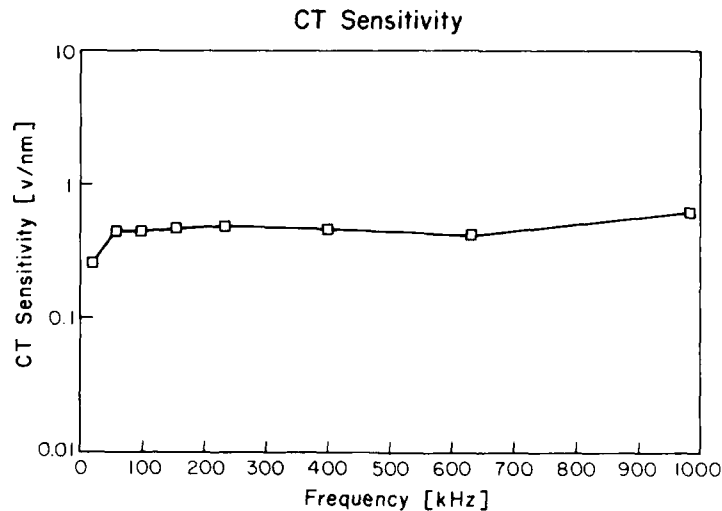


**Fig. 4.** Sensitivity of the CT versus frequency. Surface displacements were generated by a resonating rod excited by a piezoelectric transducer. The displacements were calibrated using a Michelson interferometer. The CT's response to the resonating rod was then measured to obtain a calibration of the CT.

frequency (to about 1 MHz, our range of interest for this experiment). A more complete calibration of the CT has been completed and is forthcoming.

Data from the CT is recorded on a digital oscilloscope and subsequently transferred to a workstation class computer. Time-signal averaging as well as discrete Fourier transform analysis is used in the interpretation of the data.

### *The Samples*

All samples consist of standard window pane, float glass, with crosssections of 25.4 mm high by 5.6 mm wide and varying lengths. The glass has the following properties: compressional wave velocity of 5.64 mm/ $\mu$ s, shear wave velocity of 3.35 mm/ $\mu$ s, and density of 2610 kg/m<sup>3</sup> which corresponds to a Young's modulus of 72 GPa, and a Poisson's ratio of 0.228.

The manner in which the largest sample (2.28 m long) is supported is illustrated in Fig. 1. Urethane foam is used to acoustically isolate the sample from the aluminum support structure. After initial experiments to test the experimental set-up, a vertical cut 6 mm deep and 0.5 mm wide was made in the sample 1.4 m from one end, effectively creating a configuration suitable to detect the surface breaking crack (see Fig. 7). Shorter samples were used and supported in a manner which allowed access to both the top and bottom of the sample.

### *Experimental Results*

*In support of the theoretical treatment.* The two dimensionality assumption was validated through moving the point source across the width of the sample

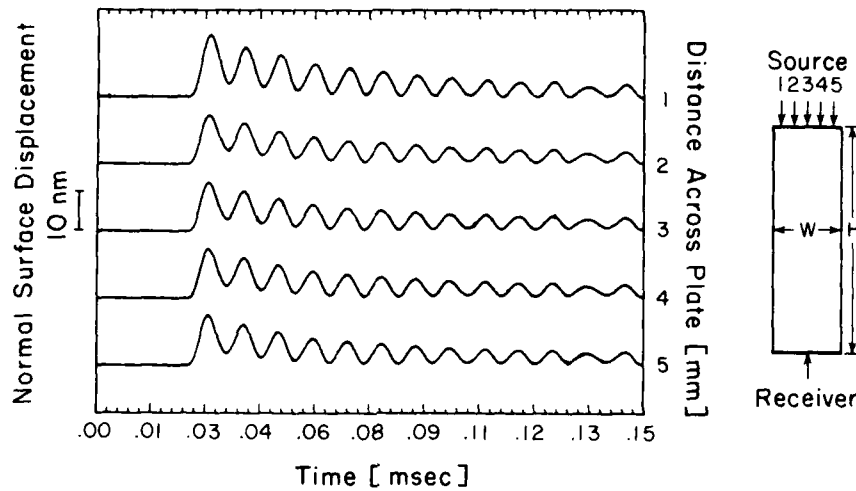


**Fig. 5.** Confirmation of two-dimensional plate assumption. The impact point of the steel bearings is moved across the 5.6 mm sample in 1 mm increments. No appreciable difference was observed unless the balls were glancing off the edge of the sample.

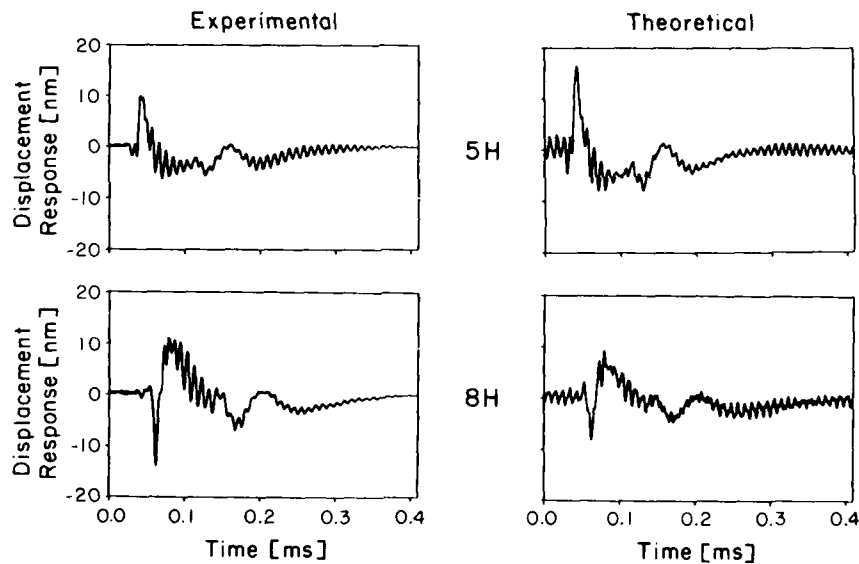


**Fig. 6.** Experimental data and theoretical simulation of the surface displacement at 5H and 8H without a crack. The experimental traces are multiplied with a cosine window to ease theoretical computation. The experimental surface response at 5H was used with the Green's function to compute the source function. This source function was then used for modeling the surface displacement at 8H. The analogous technique was used to calculate the surface displacement at 5H.

and observing the signal resulting from these impacts. Fig. 5 shows the experimental arrangement as well as the observed signals. After propagating through the thickness of the sample the signal has two-dimensional character, i.e., it is independent of where it originates along the width of the sample.

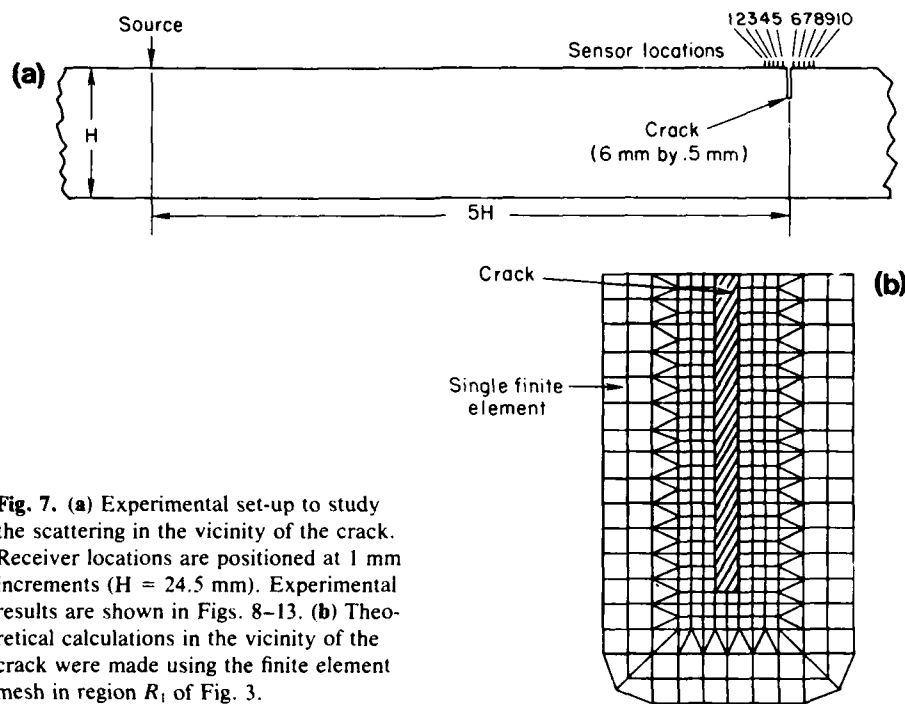


**Fig. 7.** (a) Experimental set-up to study the scattering in the vicinity of the crack. Receiver locations are positioned at 1 mm increments ( $H = 24.5$  mm). Experimental results are shown in Figs. 8–13. (b) Theoretical calculations in the vicinity of the crack were made using the finite element mesh in region  $R_1$  of Fig. 3.

The nature of the source, the impact of a steel ball bearing, is inherently simple. Its shape under the two-dimensional assumption was determined from signals recorded at  $5H$  and  $8H$  from the source ( $H$  is the thickness of the sample 25.4 mm, see Fig. 7). These experimentally observed signals together with their theoretical counterparts are shown in Fig. 6. The experimental results at  $5H$  were used with the Green's function to compute the source function. This source function was then used for modeling the surface displacement at  $8H$ . The same technique was used to calculate the theoretical surface displacement at  $5H$ .

Scattering in the far field was examined with the arrangement shown in Fig. 7. The source was located at a distance  $5H$  from the crack. The receiver was positioned at  $5H - 5$  mm to  $5H + 5$  mm in 1 mm intervals. The measured surface displacements for the cases with the crack and without the crack are shown in Fig. 8. The surface displacement changes only very little over this range if no crack is present. The forward scattering is the most notable effect of the crack (receiver locations 6–10). Amplitude spectra were calculated for each trace to allow comparison with the theoretical calculations. Figure 9 shows the spectra of the surface displacements at the positions  $5H + 1$  mm and  $5H - 1$  mm with and without the crack respectively. The experimental data as well as the theoretical results are shown. The experimental spectra were normalized to their maximum value and the theoretical values were scaled in such a way that the value at 44 kHz is identical with the experimental value. Fig. 10 shows the same spectra in the range 100 kHz to 200 kHz. It is this frequency range where the introduction of the crack causes the greatest changes in the spectra.

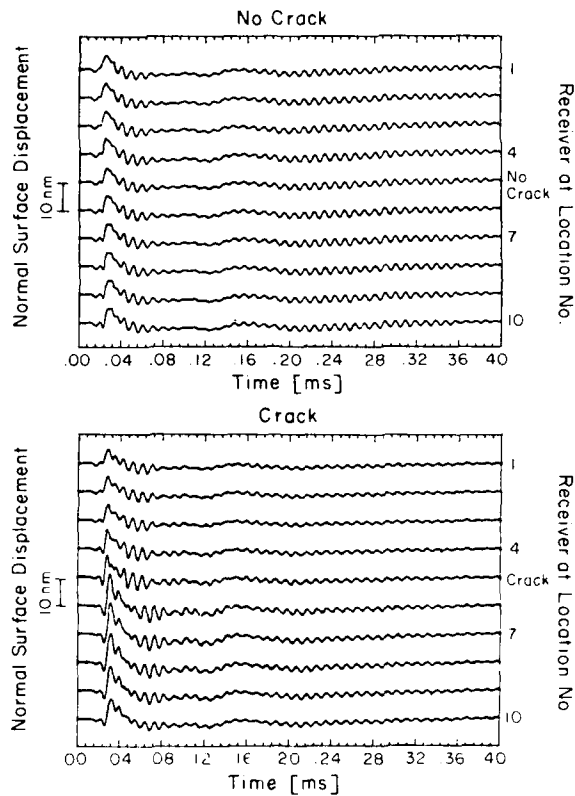


**Fig. 8.** Normal surface displacements as a function of time with and without a crack. The displacements were measured over 5 mm on either side of the crack at 1 mm intervals. The source was 5H ( $H = 25.4$  mm) from the crack position. The upper figure shows the results without a crack and the lower figure with a crack (See Fig. 7. for experimental set-up).

The ratio of the spectra at the positions  $5H - 1$  mm and  $5H + 1$  mm with and without the crack are shown in Fig. 11. In Fig. 12 the ratio of the spectra for the no-crack and the crack case are given for the positions  $5H - 1$  mm and  $5H + 1$  mm. Both representations show a distinctive change in the spectrum in the frequency range 100 kHz to 300 kHz. In Fig. 13 experimentally obtained spectral amplitudes are plotted as a function of receiver position. Each trace is normalized to its maximum value. The presence of the crack introduces a distinctive maximum of the spectral amplitudes in certain frequency ranges.

*In search of a crack.* To complement the two-dimensional far field studies reported in the previous section, we performed two additional experiments. In

**Fig. 9.** Amplitude spectra of normal surface displacements 1 mm on either side of 5H from the source with and without a crack. 5H is the distance between the source and the crack. Movement of the receiver location by 2 mm changes the amplitude spectrum very little without a crack (bottom figures) and an appreciable amount with a crack (top figures). The solid lines are experimental data, the crosses are the theoretical results.

**Fig. 10.** Amplitude spectra of Fig. 9. shown expanded between 100 kHz and 200 kHz where the crack causes the greatest changes in the spectra.

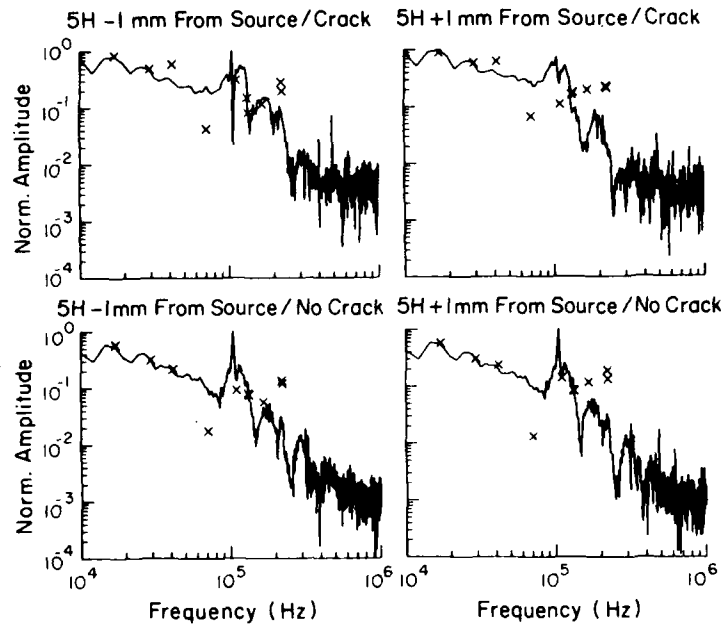


Fig. 9

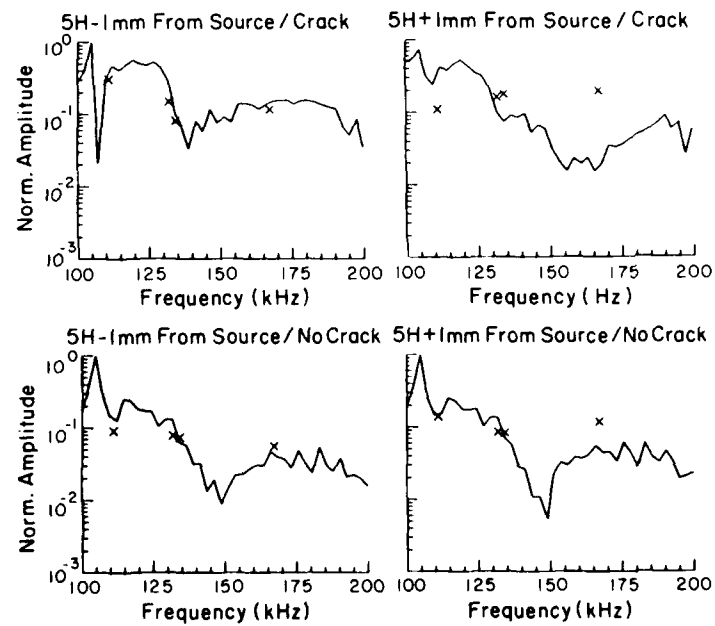
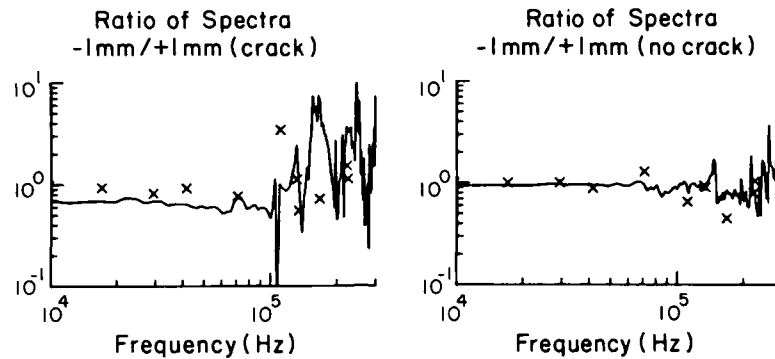
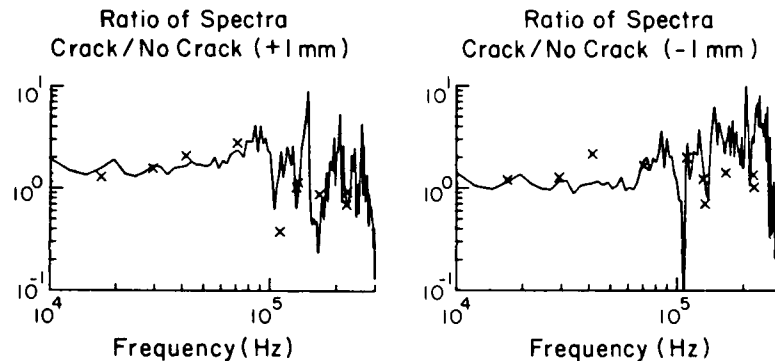


Fig. 10

See previous page for figure captions.



**Fig. 11.** Ratio of the spectra at position  $5H - 1$  mm and position  $5H + 1$  mm without a crack and with the crack.



**Fig. 12.** Ratio of the spectra with a crack and without a crack at position  $5H - 1$  mm and position  $5H + 1$  mm.

one case the source was stationary and the receiver was moved in large intervals (40 mm, nearly  $2H$ ) across the sample. In the data shown in Fig. 14 the ultimate crack, i.e., the end of the sample, is clearly visible. No effect of the induced crack is discernable however. We confirm that indeed to find small cracks one must look in detail on a scale that is on the order of the crack whether that is in the far field as described above or in the near field as we describe now.

For the near field experiments we placed the receiver and the source on opposite sides of the sample in order to observe the near field. The base plate of our transducer does not allow the source to be closer than approximately 50 mm from the receiving probe when both receiver and source are on the same surface. Figure 15 shows the recorded surface displacements if no crack is present over a distance of 180 mm from the source position.

In Fig. 16 we show the experimental set-up which we used to search for the



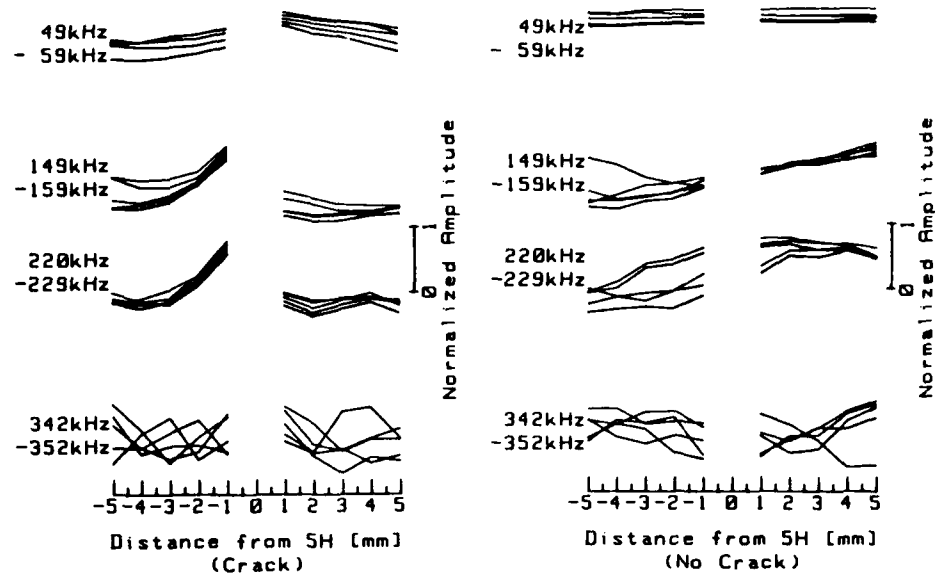


Fig. 13. Amplitude variation of several frequency groups as a function of position on the sample. The spectra were produced from the traces shown in Fig. 8.

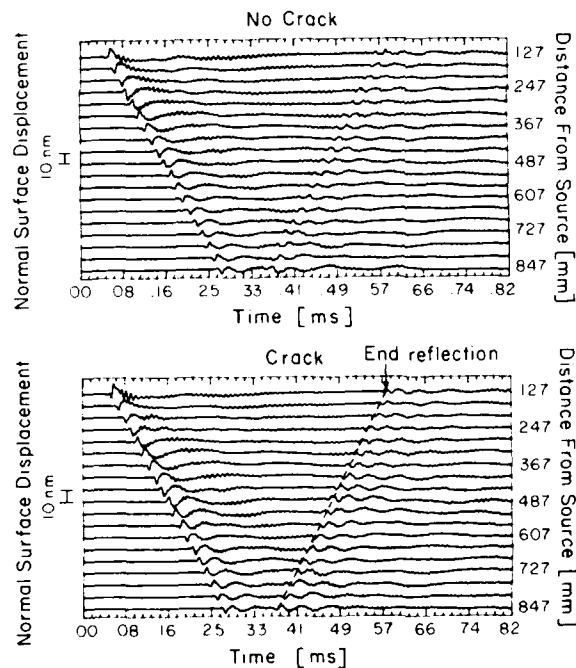
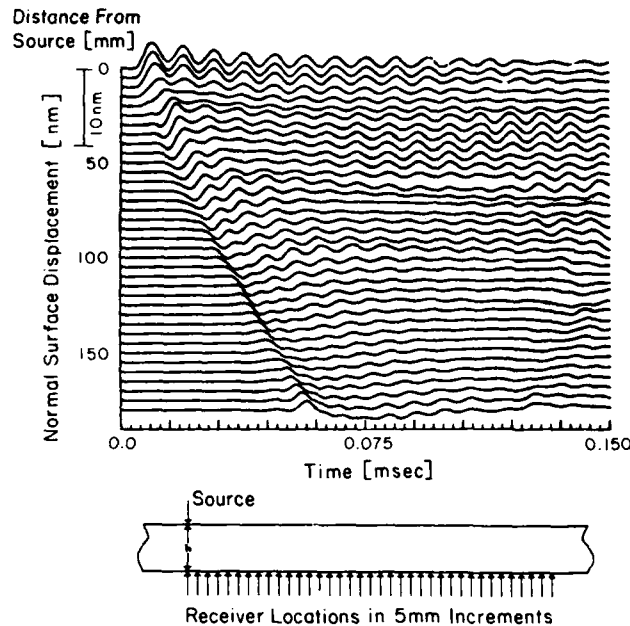
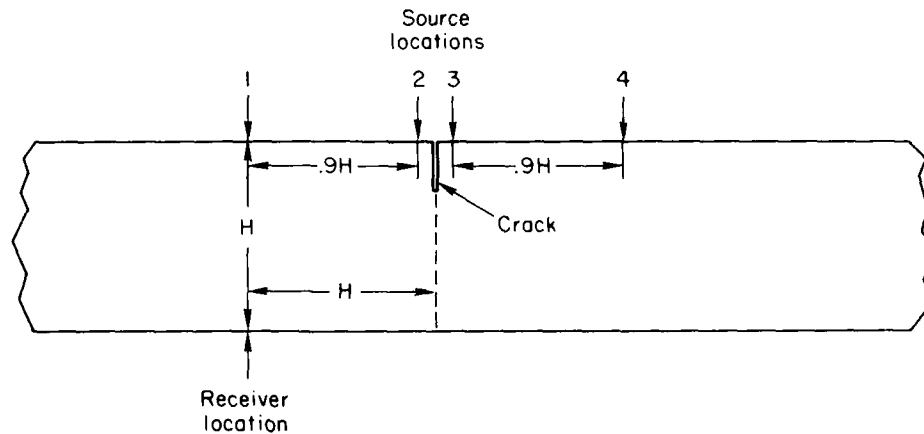


Fig. 14. Normal surface displacements as a function of time with and without a crack. The normal surface movements were measured at 40 mm intervals without a crack (top) and with a crack (bottom). The distance between the first receiver position and the source was 5H in both cases. In the lower figure the crack was located 1 mm beyond the first measurement location. While the reflection from the end of the sample is recognizable no difference in the waveforms due to the crack is perceptible.

crack in the near field. Fig. 17 shows the two sets of four traces recorded for the cases with and without a crack. The differences between the two data sets are striking. The crack is easily detectable. In traces 2 and 3 and to a lesser extent



**Fig. 15.** Near field experiment in the no-crack case.



**Fig. 16.** Experimental configuration used to study the effect of the crack. Normal surface displacements on the bottom of the sample are measured in response to ball bearing impacts at locations 1, 2, 3, and 4 above the sample. The results are illustrated in Fig. 17.

in trace 4 the presence of the crack prevents the destructive interference which occurs during the first 0.03 ms in its absence. For the no-crack case the data in Fig. 17 represents a subset of those shown in Fig. 15. There too, the regions are clearly recognizable over which the destructive interferences occur, i.e., at the 20 mm and 25 mm traces and again at the 45 mm and 50 mm traces.

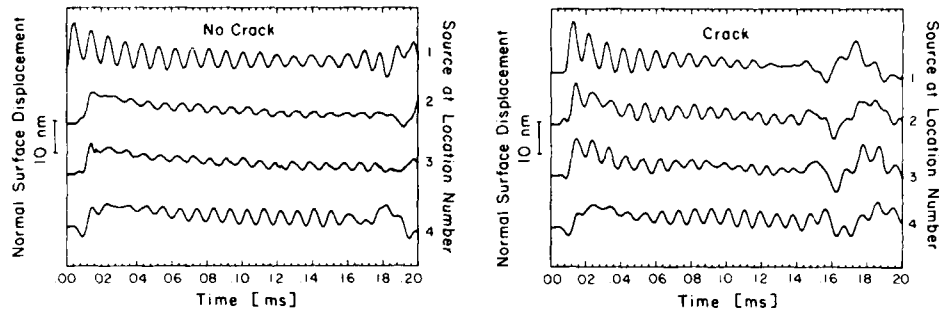


**Fig. 17.** Normal surface displacements on the opposing side of the sample from the source. The source is placed at one of the four positions shown in Fig. 16. The receiver is stationary and on the opposite side of the sample. Times after 0.12 ms are subject to reflections from the ends, and should be ignored.

## Conclusions

In this study we have presented experimental and theoretical treatment of a two-dimensional wave propagation problem in a plate with and without a surface breaking crack. For the crack free case we showed good correspondence between the experimentally observed normal displacement time series and the corresponding theoretically calculated ones when the receiver was located in the far field of the source. Finite element based calculations of changes in amplitude spectra in the vicinity of a crack are generally in good agreement with experimental observations.

High detectability of the crack was achieved when the source and receiver were located in the near field of the crack. While these observations were not treated theoretically in this study, together with the theoretical work they may offer the basis for the design of a practical crack detection gauge. Both the source and the receiver could be housed in the same physical unit and thus be easily transportable and usable.

**Acknowledgments.** The following persons were instrumental in the completion of this project: Tapes Chakraborty, Henrietta Smith, Ivan Getting, Mounir Bouden, and Edward Field. The experimental work was carried out in the Geophysics research facilities at the Cooperative Institute for Research in Environmental Sciences, University of Colorado, Boulder. The theoretical work was carried out in the Mechanical Engineering research facilities at the University of Colorado, Boulder. Numerical computations were carried out by the National Center for Supercomputing Applications at the University of Illinois, Urbana. The work was funded by grants from the Office of Naval Research (#N00014-86-K-0280; Scientific Officer: Dr. Y. Rajapakse), the National Science Foundation (#MSM-86-09813) and NASA (#NAGW-1388).

## Appendix I

Let us write

$$a = k_{2m}^2 - 2k^2, \quad b = 2k\eta_{1m}, \quad c = 2k\eta_{2m}$$

Then the matrix  $[l^m(z)]$  have the elements

$$\begin{aligned}
 l_{11}^m &= ike^{i\eta_{1m}z}, l_{12}^m = -i\eta_{2m}e^{i\eta_{2m}z} \\
 l_{13}^m &= ike^{i\eta_{1m}(h-z)}, l_{14}^m = i\eta_{2m}e^{i\eta_{2m}(h-z)} \\
 l_{21}^m &= i\eta_{1m}e^{i\eta_{1m}z}, l_{22}^m = ike^{i\eta_{2m}z} \\
 l_{23}^m &= -i\eta_{1m}e^{i\eta_{1m}(h-z)}, l_{24}^m = ike^{i\eta_{2m}(h-z)} \\
 l_{31}^m &= -a\mu_me^{i\eta_{1m}z}, l_{32}^m = -c\mu_me^{i\eta_{2m}z} \\
 l_{33}^m &= -a\mu_me^{i\eta_{1m}(h-z)}, l_{34}^m = c\mu_me^{i\eta_{2m}(h-z)} \\
 l_{41}^m &= -b\mu_me^{i\eta_{1m}z}, l_{42}^m = a\mu_me^{i\eta_{2m}z} \\
 l_{43}^m &= b\mu_me^{i\eta_{1m}(h-z)}, l_{44}^m = a\mu_me^{i\eta_{2m}(h-z)}
 \end{aligned}$$

The elements of the  $4 \times 1$  matrix  $[Y_j^m]$  depend on the direction and location of the source. If the source is in the  $x$ -direction at  $(x', z')$  in the  $m^{\text{th}}$  layer then,

$$\begin{aligned}
 Y_{11}^m &= ikA^{1m}e^{i\eta_{1m}|z-z'|} - i\eta_{2m}B^{1m}e^{i\eta_{2m}|z-z'|} \\
 Y_{21}^m &= \pm i\eta_{1m}A^{1m}e^{i\eta_{1m}|z-z'|} \pm ikB^{1m}e^{i\eta_{2m}|z-z'|} \\
 \frac{1}{\mu_m} Y_{31}^m &= -aA^{1m}e^{i\eta_{1m}|z-z'|} - cB^{1m}e^{i\eta_{2m}|z-z'|} \\
 \frac{1}{\mu_m} Y_{41}^m &= \mp bA^{1m}e^{i\eta_{1m}|z-z'|} \pm aB^{1m}e^{i\eta_{2m}|z-z'|}
 \end{aligned}$$

On the other hand, for the force in the  $z$ -direction we have,

$$\begin{aligned}
 Y_{13}^m &= \pm ikA^{3m}e^{i\eta_{1m}|z-z'|} \mp i\eta_{2m}B^{3m}e^{i\eta_{2m}|z-z'|} \\
 Y_{23}^m &= i\eta_{1m}A^{3m}e^{i\eta_{1m}|z-z'|} + ikB^{3m}e^{i\eta_{2m}|z-z'|} \\
 \frac{1}{\mu_m} Y_{33}^m &= \mp aA^{3m}e^{i\eta_{1m}|z-z'|} \pm cB^{3m}e^{i\eta_{2m}|z-z'|} \\
 \frac{1}{\mu_m} Y_{43}^m &= -bA^{3m}e^{i\eta_{1m}|z-z'|} + aB^{3m}e^{i\eta_{2m}|z-z'|}
 \end{aligned}$$

## References

1. R.D. Mindlin. In: *Structural Mechanics*, edited by J.N. Goodier and N.J. Hoff. Pergamon, New York (1960)
2. A.N. Ceranoglu and Y.H. Pao. *J. Appl. Mech.* **48**: 125 (1981)
3. N.N. Hsu, J.A. Simmons, and S.C. Hardy. *Mat. Eval.* **325**: 100 (1977)
4. J. Miklowitz. *The Theory of Elastic Waves and Waveguides*. North-Holland Publishing Amsterdam (1978)
5. Y.H. Pao. *Theory of Acoustic Emission, Elastic Waves and Nondestructive Testing of Materials*. American Society of Mechanical Engineering, New York **29**: 85 (1978)

6. N.N. Hsu and S.C. Hardy. In: *Elastic Waves and Non-destructive Testing of Materials*, edited by Y.H. Pao. American Society of Mechanical Engineering, New York **29**: 85 (1978)
7. Y.H. Pao, R. Gajewski, and A.N. Ceranoglu. *J. Acoust. Soc. Am.* **65**: 96 (1979)
8. R.L. Weaver and Y.H. Pao. *J. Appl. Mech.* **49**: 821 (1982)
9. N. Vasudevan and A.K. Mal. *J. Appl. Mech.* **52**: 356 (1986)
10. J.E. Michaels, T.E. Michaels, and W. Sachse. *Mat. Eval.* **39**: 1032 (1981)
11. C.B. Scruby, H.N.G. Wadley, R.J. Dewhurst, D.A. Hutchins, and S.B. Palmer. *Mat. Eval.* **39**: 1250 (1981)
12. N.N. Hsu and F.R. Breckenridge. *Mat. Eval.* **39**: 60 (1981)
13. T.M. Procter, F.R. Breckenridge, and Y.H. Pao. *J. Acoust. Soc. Am.* **74**: 1905 (1983)
14. C. Chang and W. Sachse. *J. Acoust. Soc. Am.* **77**: 1335 (1985)
15. J.E. Michaels and Y.H. Pao. *J. Acoust. Soc. Am.* **77**: 2005 (1985)
16. J.E. Michaels and Y.H. Pao. *J. Appl. Mech.* **53**: 61 (1986)
17. A.K. Mal. *Int. J. Eng. Sci.* **26**: 257 (1988)
18. J.D. Achenbach. *Wave Propagation in Elastic Solids*. North-Holland Publishing, Amsterdam (1973)
19. P.C. Xu and A.K. Mal. *Wave Motion* **7**: 235 (1985)
20. K.R. Khair and S.K. Datta. *Advances in Fracture Research* **5**: 3175 (1989)
21. K.R. Khair, S.K. Datta, and A.H. Shah. *Bull. Seismo. Soc. Am.* (in press)
22. F.M. Boler, H. A. Spetzler, and I.C. Getting. *Rev. Sci. Instr.* **55**: 1293 (1984)

Accession For	
NTIS CRA&I	<input checked="" type="checkbox"/>
DTIC TAB	<input type="checkbox"/>
Unannounced	<input type="checkbox"/>
Justification	
By	
Distribution /	
Availability Codes	
Dist	Avail and/or Special
A-1	21

